





Quasiparticle band structure and excitonic optical response in V_2O_5 bulk and monolayer

Claudio Garcia ¹, Santosh Kumar Radha ², Swagata Acharya ³, and Walter R. L. Lambrecht ^{1,*}

¹*Department of Physics, Case Western Reserve University, Cleveland, Ohio-44106-7079, USA*

²*Agnostiq Inc. Toronto, Ontario, Canada M5V 2Y1*

³*National Renewable Energy Laboratory, Golden, Colorado 80401, USA*



(Received 18 March 2024; revised 17 May 2024; accepted 17 July 2024; published 1 August 2024)

The electronic band structure of V_2O_5 is calculated using an all-electron quasiparticle self-consistent (QS) GW method, including electron-hole ladder diagrams in the screening of W , named $QSG\hat{W}$ and using a full-potential linearized muffin-tin-orbital basis set. The optical dielectric function calculated with the Bethe-Salpeter equation (BSE) exhibits excitons with large binding energy, consistent with spectroscopic ellipsometry data and other recent calculations using a pseudopotential plane-wave-based implementation of the many-body-perturbation theory approaches. Convergence issues are discussed. Sharp peaks in the direction perpendicular to the layers at high energy are found to be an artifact of the truncation of the numbers of bands included in the BSE calculation of the macroscopic dielectric function. The static (electronic screening only) dielectric constant $\epsilon_1(\omega = 0)$ gives indices of refraction in good agreement with experiment. The exciton wave functions are analyzed in various ways. They correspond to charge transfer excitons with the hole primarily on oxygen and electrons on vanadium, but depending on which exciton, the distribution over different oxygens changes. The dark exciton at 2.6 eV is the most localized and has the highest weight on the bridge oxygen, while the lowest bright excitons for in-plane polarizations at 3.1 eV for $\mathbf{E} \parallel \mathbf{a}$ and 3.2 eV for $\mathbf{E} \parallel \mathbf{b}$ have their higher weight on the chain and vanadyl oxygens. The exciton wave functions have a spread of about 5–15 Å, with asymmetric character for the electron distribution around the hole depending on which oxygen the hole is fixed at. The same method applied first to bulk layered V_2O_5 is here applied to monolayer V_2O_5 . The monolayer quasiparticle gap increases inversely proportional to interlayer distance once the initial interlayer covalent couplings are removed which is thanks to the long-range nature of the self-energy and the reduced screening in a two-dimensional system. The optical gap on the other hand is relatively independent of interlayer spacing because of the compensation between the self-energy gap shift and the exciton binding energy, both of which are proportional to the screened Coulomb interaction \hat{W} . Recent experimental results on very thin layer V_2O_5 obtained by chemical exfoliation provide experimental support for an increase in gap.

DOI: [10.1103/PhysRevB.110.085102](https://doi.org/10.1103/PhysRevB.110.085102)

I. INTRODUCTION

Exciton binding energies in some layered transition metal oxides were recently found to be extremely high, exceeding 1.0 eV [1,2]. This is related to the relatively low dispersion band edges in these materials and the low screening of the Coulomb interaction in ionic materials, which suggest a Frenkel type exciton. V_2O_5 is one such layered material for which it was recently found that the excitons not only have strong binding energy but for which these excitons nonetheless exhibit not so strongly localized spatial extent and with an anisotropic delocalization in unexpected directions [2].

The band gap in V_2O_5 has presented a puzzle for several years, since the first GW calculations were performed. While local density approximation (LDA) calculations [3] gave results close to the experimentally accepted gap of about 2.3 eV, which was extracted from Tauc plots of the optical absorption [4], quasiparticle self-consistent (QS) GW calculations gave a much larger band gap exceeding 4 eV [5]. These results

were also confirmed by other G_0W_0 implementations [6,7]. This puzzle was recently resolved by showing that including electron-hole effects in the dielectric function using the Bethe-Salpeter-Equation (BSE) approach [2] gives good agreement with spectroscopic ellipsometry and reflectivity data [8,9]. These data show indeed sharp excitonic peaks with the lowest one at about 3.1 eV for $\mathbf{E} \parallel \mathbf{a}$. The lower gap extracted from optical absorption is still not completely understood and may either result from excitons related to the indirect gap or phonon-mediated activation of a dark exciton [10].

While most GW and BSE implementations are based on pseudopotential plane-wave basis set implementations, all-electron implementations of many-body perturbation theory have recently become possible with linearized muffin-tin-orbital and linearized augmented plane-wave basis sets [11–17]. The BSE approach was recently implemented using this approach by Cunningham *et al.* [18,19]. An all-electron implementation is, in principle, preferable since it avoids the uncertainties related to choosing pseudopotentials and describes the core-valence exchange more accurately. Our first goal with the present paper is to check whether similar strong

*Contact author: walter.lambrecht@case.edu

excitons are obtained with an all-electron BSE implementation and to further check the consistency of the QSGW band gap between all-electron- and pseudopotential-based implementations. Furthermore, in the usual QSGW approach and also in G_0W_0 approaches, W is calculated in the random-phase approximation (RPA), meaning that the polarization propagator is calculated as $P(1, 2) = -iG(1, 2)G(1, 2)$ in terms of the Green's function and is thus represented by a simple bubble diagram. (Here 1 is short hand for $\{\mathbf{r}_1, \sigma_1, t_1\}$ including position, spin, and time variable.) The screening is thereby underestimated because it does not include electron-hole interaction effects. This has been recognized for some time as a deficiency and has been corrected among other via an excursion into time-dependent density functional theory, including a suitable exchange correlation kernel in the calculation of the polarization propagator. Shishkin *et al.* [20] used a kernel derived from BSE calculations, while Chen and Pasquarello [21] used the bootstrap kernel. Recently Cunningham *et al.* [19] proposed an alternative method to include the ladder diagrams via a BSE formulation in terms of the four-point polarization propagator. It can be viewed also as a vertex correction in the spirit of the Hedin equations [22,23]. Unlike the approach of Kutepov [15,16], who implemented similar vertex corrections both in the screened Coulomb interaction $W = v + vPW$ with $P = -iG\Gamma G$ and the self-energy $\Sigma = -iG\Gamma\Gamma$, and works directly toward implementing the Hedin equations self-consistently, the approach of Cunningham uses the QSGW approach, in which, in each iteration, the full G is replaced by G_0 corresponding to an updated Hermitian non-interacting Hamiltonian H_0 . The idea is to make the dynamic perturbation from H_0 as small as possible by incorporating a static approximation of the self-energy into the exchange correlation potential of H_0 . The two Green's functions differ by $G = ZG_0 + \hat{G}$ with Z a quasiparticle renormalization factor and \hat{G} the incoherent part. But in Σ , Z is then largely canceled by the vertex being approximately proportional to $1/Z$, $\Gamma \propto 1/Z$. This suggests that the vertex in Σ should play a less important role in the QSGW approach [11]. In practice, it gives accurate quasiparticle gaps and optical spectra when BSE is used for the latter without vertex corrections in the self-energy [1,19]. However, it has thus far been applied only to a limited number of materials. It is thus of interest to test how it works for a challenging case like V_2O_5 .

Finally, the question arises for such layered materials, whether the band gap and optical properties will significantly change when going to the monolayer limit. From Bhandari *et al.* [5] it is clear that in the LDA only a small increase in gap occurs related to the breaking of some interlayer interactions and hence reduced dispersion of the valence band edge. However, in two-dimensional (2D) materials, one expects a strong reduction of the screening when the monolayer is isolated [24,25]. In Bhandari *et al.* [5] the QSGW gap was shown to vary as $1/L$, with L the interlayer distance, and this led to an extremely large gap but which was of course overestimated. Thus it becomes of great interest to study how the inclusion of electron-hole interactions in the form of ladder diagrams will affect the quasiparticle gap in a monolayer and how the reduced screening will affect the exciton binding energies and exciton spectrum. This is the second main goal of the present paper.

II. COMPUTATIONAL METHODS

The density functional theory (DFT) calculations and subsequent many-body-perturbation theory (MBPT) calculations are performed using the QUESTAAL suite of codes as described in Ref. [12]. These use a full-potential linearized muffin-tin-orbital basis set for the band structure calculations and an auxiliary mixed interstitial-plane-wave and muffin-tin partial wave product basis set for the representation of two point quantities [bare Coulomb $v(1, 2)$, screened Coulomb $W(1, 2)$ and polarization propagator $P(1, 2)$] in the MBPT. The details of the Hedin- GW implementation are given in Ref. [11] and for the Bethe-Salpeter-Equation approach in Cunningham *et al.* [18,19]. Briefly, in the quasiparticle-self-consistent QSGW method, a static and Hermitian $\tilde{\Sigma}_{ij} = \frac{1}{2}\text{Re}[\Sigma_{ij}(\epsilon_i) + \Sigma_{ij}(\epsilon_j)]$ exchange-correlation potential is extracted from the energy-dependent $\Sigma_{ij}(\omega)$ where the matrices are given in the basis ψ_i of the H_0 Hamiltonian. The $\tilde{\Sigma}_{ij} - v_{xc}^{\text{DFT}}$ is then added to the original H_0^{DFT} and defines an updated H_0 from which the next $\Sigma(\omega) = -iG_0(\omega) \otimes W_0(\omega)$ is obtained, where the energy-dependent self-energy $\Sigma(\omega)$ is a convolution of the one-particle Green's function and the screened Coulomb interaction. When iterated to self-consistency in $\tilde{\Sigma}$, the quasiparticle energies become the same as the Kohn-Sham eigenvalues of the H_0 and the results are independent of the starting H_0^{DFT} . Here we use the generalized gradient approximation (GGA) in the Perdew-Burke-Ernzerhof [26] functional as starting DFT.

The screened Coulomb interaction $W_0 = (1 - P_0^{\text{RPA}}v)^{-1}v$ is normally obtained from P_0^{RPA} in the RPA $P_0^{\text{RPA}} = -iG_0G_0$ (i.e., using only the bubble diagram). The subscript 0 indicates that it is calculated from the eigenstates of H_0 . Instead, in the QSGW method, the polarization propagator used is P , which includes a summation over ladder diagrams instead of only the bubble diagram. This is done by converting to the four-particle generalized susceptibility P and solving a Bethe-Salpeter equation and then converting back to the two-particle representation,

$$P(12) = P^{\text{RPA}}(12) - \int d(34)P^{\text{RPA}}(1134)W(34)P(3422), \quad (1)$$

with $P^{\text{RPA}}(1234) = -iG(13)G(42)$. In practice this is done expanding the four-point quantities in the basis set of single particle eigenfunctions and amounts to diagonalizing an effective two-particle Hamiltonian. It should be noted, however, that this involves solving a BSE at a mesh of \mathbf{q} points because in GW we need $W(\mathbf{q}, \omega)$. A static approximation is made for W in Eq. (1) and the Tamm-Dancoff approximation (TDA) is made. We note, however, that this static, i.e., $\omega = 0$ approximation is only made in Eq. (1) for W but the frequency dependence is maintained in the final P through that of P^{RPA} . Thus the final $W = (1 - vP)^{-1}v$ used in the QSGW equations is of course ω dependent.

This approach is equivalent to adding a vertex correction to P in the Hedin set of equations as explained for example in Refs. [27,28]. Details of the implementation and its justification are discussed in Refs. [1,19].

Once the band structure is obtained in the QSGW or QSGW method approximations, from which we obtain the

fundamental or quasiparticle gap, we can calculate the macroscopic dielectric function $\epsilon_M(\omega)$ for $\mathbf{q} \rightarrow 0$. This involves another BSE equation with the kernel

$$K(1234) = \delta(12)\delta(34)\bar{v} - \delta(13)\delta(24)W, \quad (2)$$

with \bar{v} the microscopic part of the bare Coulomb interaction v , i.e., omitting the long-range $\mathbf{G} = 0$ part in a Fourier expansion. This is again done in the TDA and with a static $\hat{W}(\omega = 0)$. Here the first term in the kernel provides the local field corrections and the second provides the electron-hole interaction effects. Expanding this four-point quantity in the basis of one-particle eigenstates $\psi_{n\mathbf{k}}(\mathbf{r})$, one obtains an effective two-particle Hamiltonian, given by

$$H_{n_1 n_2 \mathbf{k}, n'_1 n'_2 \mathbf{k}'}^{(2p)}(\mathbf{q}) = (\epsilon_{n_2 \mathbf{k} + \mathbf{q}} - \epsilon_{n_1 \mathbf{k}}) \delta_{n_1 n'_1} \delta_{n_2 n'_2} \delta_{\mathbf{k} \mathbf{k}'} - (f_{n_2 \mathbf{k} + \mathbf{q}} - f_{n_1 \mathbf{k}}) K_{n_1 n_2 \mathbf{k}, n'_1 n'_2 \mathbf{k}'}(\mathbf{q}) \quad (3)$$

with $f_{n\mathbf{k}}$ the Fermi occupation function for band n at \mathbf{k} . Diagonalizing this Hamiltonian in the Tamm-Dancoff approximation, where n_1 is restricted to be a valence state and n_2 a conduction band state, one obtains the exciton eigenvalues $E^\lambda(\mathbf{q})$ and eigenvectors $A_{n_1 n_2 \mathbf{k}}^\lambda(\mathbf{q})$. Introducing the shorthand $s = \{n_1 n_2 \mathbf{k}\}$, the dielectric function is then given by

$$\epsilon_M(\omega) = 1 - \lim_{\mathbf{q} \rightarrow 0} \frac{8\pi}{|\mathbf{q}|^2 \Omega N_k} \sum_{ss'} (f_{n_2 \mathbf{k}' + \mathbf{q}} - f_{n_1 \mathbf{k}'}) \times \rho_s(\mathbf{q}) \sum_{\lambda} \frac{A_s^\lambda(\mathbf{q}) A_s^{\lambda*}(\mathbf{q})}{E^\lambda(\mathbf{q}) - \omega \pm i\eta} \rho_{s'}(\mathbf{q})^* \quad (4)$$

with the matrix element

$$\rho_{n_1 n_2 \mathbf{k}}(\mathbf{q}) = \langle \psi_{n_2 \mathbf{k} + \mathbf{q}} | e^{i\mathbf{q} \cdot \mathbf{r}} | \psi_{n_1 \mathbf{k}} \rangle. \quad (5)$$

Here we have assumed no spin polarization and a factor two for spin and N_k is the number of \mathbf{k} points in the Brillouin zone. The limit $\mathbf{q} \rightarrow 0$ can be taken analytically, $e^{i\mathbf{q} \cdot \mathbf{r}} \approx 1 + i\mathbf{q} \cdot \mathbf{r}$ and then involves dipole matrix elements $\langle \psi_{n_2 \mathbf{k}} | \mathbf{r} | \psi_{n_1 \mathbf{k}} \rangle \cdot \hat{\mathbf{q}}$, where $\hat{\mathbf{q}}$ gives the direction along which we take the limit to zero and which corresponds to the polarization directions of the macroscopic tensor $\epsilon_M(\omega)$. Finally, one converts the dipole matrix elements between Bloch states to velocity matrix elements divided by the band difference, $\langle \psi_{n_2 \mathbf{k}} | [H, \mathbf{r}] | \psi_{n_1 \mathbf{k}} \rangle = (\epsilon_{n_2 \mathbf{k}} - \epsilon_{n_1 \mathbf{k}}) \langle \psi_{n_2 \mathbf{k}} | \mathbf{r} | \psi_{n_1 \mathbf{k}} \rangle$ and we then only need to diagonalize $H^{(2p)}(\mathbf{q})$ at $\mathbf{q} = 0$.

Besides shifts of the oscillator strength in the continuum, it can lead to bound excitons below the quasiparticle gap. The lowest bright excitons provide the exciton gap. At present, only direct dipole matrix elements are included between the one-particle states, so we only obtain direct excitons. Lower indirect excitons which would involve a phonon assisted transition could exist but are not calculated here. The exciton eigenstates are a mixture of the vertical transition (between valence v and conduction c band states at a fixed \mathbf{k}), given by

$$\Psi^\lambda(\mathbf{r}_h, \mathbf{r}_e) = \sum_{v\mathbf{k}c\mathbf{k}} A_{v\mathbf{k}c\mathbf{k}}^\lambda \psi_{v\mathbf{k}}(\mathbf{r}_h) \psi_{c\mathbf{k}}(\mathbf{r}_e) \quad (6)$$

with $\mathbf{r}_h, \mathbf{r}_e$ the hole and electron position of the electron-hole pair bound in the exciton. The summation over \mathbf{k} can lead to dark excitons if $A_{v\mathbf{k}c\mathbf{k}}^\lambda$ at symmetry equivalent \mathbf{k} cancel each other even if the dipole matrix elements between these states are not zero at \mathbf{k} . The coefficients $A_{v\mathbf{k}c\mathbf{k}}^\lambda$, which are the

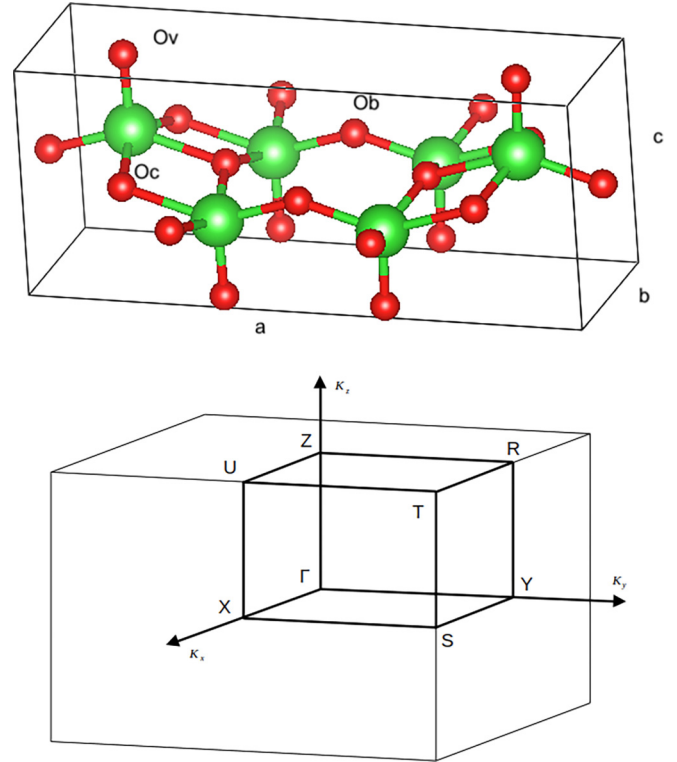


FIG. 1. Crystal structure (top) and Brillouin zone (bottom) of V_2O_5 .

eigenvectors of the two-particle Hamiltonian can be used to ascertain, which band pairs vc and at which \mathbf{k} points contribute to a given exciton. The exciton wave-function modulo squared gives the probability to find the electron at position \mathbf{r}_e for a fixed \mathbf{r}_h or vice versa and is used to visualize the exciton spatial extent.

Further detail of the calculations are as follows. We use a *spdfspd* basis set on V and O atoms, meaning that two sets of Hankel function energy κ^2 and smoothing radius R_{sm} are used for the envelope functions of the LMTO basis set and with angular momenta up to $l = 3$ for the first set and $l = 2$ for the second set. Inside the spheres, the basis functions are augmented by radial functions up to $l_{\text{maxa}} = 4$ and V_{3p} semicore orbitals are treated as local orbitals, which means they are included in the basis set rather than in the core but have only an on-site contribution and are not augmented into other spheres. We use slightly different muffin-tin spheres for the chemically different O atoms optimized to avoid overlap between muffin-tin spheres. These are standard, well converged settings of the basis set. The *GW* self-energy matrix is calculated up to a maximum energy of 2.56 Ry and approximated by an average diagonal value above it as explained in Ref. [11]. Other details of the implementation, such as the construction of the mixed product basis set, which determines the dynamical screening, the contour integration approach for the self-energy and the offset Γ method used to deal with the $\mathbf{q} \rightarrow 0$ integrable divergence of W all follow the approaches explained in Refs. [11,29].

The experimental structure in the *Pmnm* space group is used as reported by Enjalbert and Galy [30] and with lattice

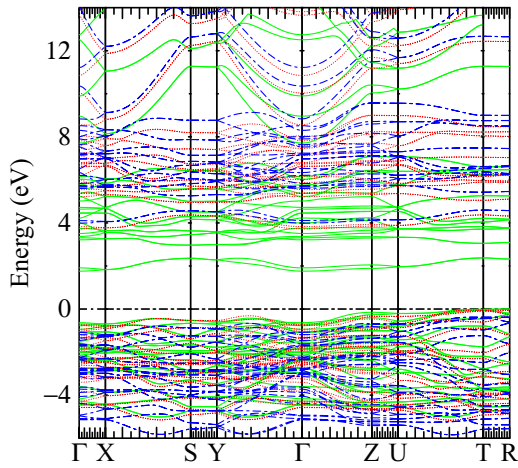


FIG. 2. Band structure of V_2O_5 in GGA (green solid), QSGW (blue dashed), and $QSG\hat{W}$ (red dotted) lines. The zero is placed at the VBM of GGA.

constants $a = 11.512 \text{ \AA}$, $b = 3.564 \text{ \AA}$, and $c = 4.368 \text{ \AA}$. The structure is shown in Fig. 1 and consist of weakly van der Waals bonded layers, in the c direction and double zigzag V-O chains in the ab -plane along b . The O in the chain are called chain oxygen, O_c and the chains are connected by bridge oxygens O_b . The vanadyl oxygens O_v are bonded to a single V and point alternating up and down along the chains but in the same direction across a bridge or rung of the ladders. This is called a ladder compound with ladders consisting of the V- O_b -V rungs. Each V is surrounded by an approximately square pyramid of five oxygens, one O_v , one O_b , and three O_c . The corresponding Brillouin zone labeling is also shown in Fig. 1.

III. RESULTS

A. Bulk

1. Band structure

First we show the band structure obtained in the GGA, QSGW, and $QSG\hat{W}$ approximations in Fig. 2. The zero is placed at the valence band maximum (VBM) of the GGA. We can thus see how the GW separately shifts valence bands down and conduction bands up. This assumes the charge density is not changing too much between them. We can see that the gap correction from GGA to QSGW occurs primarily in the conduction band. When adding the ladder diagrams, the VBM shifts back almost to the GGA position and the conduction band minimum (CBM) goes down slightly. The gaps are given in Table I. Our present QSGW calculation differs from the older one by Bhandari *et al.* [5,31] in using a more complete basis set including f orbitals. The CBM occurs at Γ , the VBM at T , the lowest direct gap at Z . We give the indirect gap $\Gamma - T$, the lowest direct gap at Z and the direct gap at Γ . We can see that the inclusion of ladder diagrams reduces the gap correction beyond GGA by a factor ~ 0.77 , close to a factor 0.8 as has been observed before for many other materials [32]. Interestingly, our all-electron $QSG\hat{W}$ gaps agree closely with the QSGW pseudopotential gaps of Gorelov *et al.* [2]. This indicates that the screening of W at the RPA levels is slightly

TABLE I. Band gaps in eV for bulk V_2O_5 .

Method	Indirect	Minimum direct	Direct at Γ
GGA	1.759	2.041	2.392
QSGW	4.370	4.799	5.075
$QSG\hat{W}$	3.781	4.178	4.452
$QSGW$ -pseudo ^a	3.8		4.4
$E_g(QSG\hat{W}) - E_g(GGA)$	0.774	0.775	0.768
$E_g(QSG\hat{W}) - E_g(GGA)$			
$QSGW$ ^b	4.00	4.45	4.83

^aFrom Gorelov *et al.* [2].

^bFrom Bhandari *et al.* [5] and [31].

underestimated in Ref. [2] compared to ours and this error is almost the same as the subsequent reduction of W to \hat{W} due to the inclusion of electron-hole interactions via ladder diagrams.

2. Imaginary part of the dielectric function

Next, in Fig. 3 we show the macroscopic dielectric function in the IPA and BSE both using the $QSG\hat{W}$ bands. We can see that the BSE strongly alters the dielectric function and exciton peaks with large binding energies appear significantly below the quasiparticle gap. This is in good agreement with experimental results obtained from reflectivity by Mokerov *et al.* [8] and more recent spectroscopic ellipsometry results as shown in Gorelov *et al.* [2]. We also show a comparison with the BSE results by Gorelov *et al.* [2]. The agreement is quite good, considering that a completely different code is used in

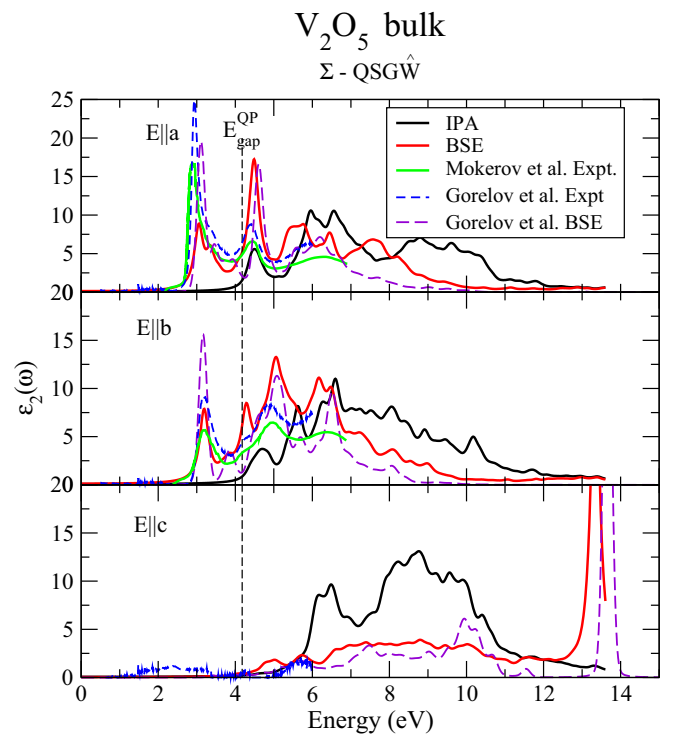


FIG. 3. Imaginary part of the dielectric function for bulk V_2O_5 for three polarization, comparing IPA to BSE and to experimental results from Mokerov *et al.* [8] and experimental and calculated data from Gorelov *et al.* [2].

that work and that the intensities in the exciton region were found to be quite sensitive to details of the calculation. Some of the differences with the work of Gorelov *et al.* [2] are that our calculation of the BSE two particle Hamiltonian includes 30 valence bands and 20 conduction bands, i.e., all O-2*p* and V-3*d* related bands, while Gorelov *et al.* used 15 valence bands and 16 conduction bands. We used a $1 \times 5 \times 5$ *k*-point mesh (our $2 \times 6 \times 6$ *k*-mesh calculation is identical with $1 \times 5 \times 5$ *k*-mesh calculation with only ~ 20 meV difference in band gap) in the BSE and *GW* calculations while Gorelov *et al.* used a $6 \times 6 \times 6$ grid. We used a smaller number of **k** points in the *a* direction because the unit cell is largest in this direction and hence the Brillouin zone is smaller in this direction. Furthermore because of the anisotropy in structure, the dispersion of the bands is larger in the *b* than the *a* or *c* directions. Although it is difficult to fully trace the differences between the pseudopotential plane-wave calculation of Gorelov *et al.* [2] and the present calculation, the main difference appears to lie in the calculation of the screened Coulomb interaction *W* or the inverse dielectric function. In the mixed product basis set representation $\varepsilon_{JJ}^{-1}(\mathbf{q}, \omega)$ the screening on small spatial scales is dealt with via products of partial waves in the spheres, which is easier to converge than by using high reciprocal lattice vectors **G** in $\varepsilon_{GG}^{-1}(\mathbf{q}, \omega)$. The virtues of the product basis set were first introduced by Aryasetiawan and Gunnarsson [33]. The idea of describing the linear response using partial wave function inside the spheres to avoid the need of high-lying band states was further elaborated in recent work by Betzinger *et al.* [34]. Thus, we guess that, in spite of the careful convergence studies of the band gap as function of number of bands at the G_0W_0 level in Ref. [2], their RPA *W* might still be slightly underestimated and agree better with our \tilde{W} . However, given a certain value of $W(\mathbf{r}, \mathbf{r}', \omega)$, which is in practice represented by a different basis set, the two totally different codes eventually agree on the quasiparticle band gaps resulting from it and the optical gap as obtained subsequently by the BSE. This indicates, that the calculation of the *GW* self-energy in terms of number of bands included as well as the BSE calculation are well converged in both approaches. While [2] used a plasmon-pole approximation, it was tested against the more rigorous contour integration approach used in the QUESTAAL code and detailed in Ref. [11]. While a pseudopotential treatment of the interaction with core and semicore states is different from an all-electron approach, it should be noted that Gorelov *et al.* included V-3*s* and V-3*p* states as valence electrons. In our approach, V-3*s* states are treated with atomic boundary conditions at the muffin-tin sphere radii while V-3*p* states are included as local orbitals. This means the 3*p* states are allowed to hybridize with the other valence states, but 3*s* states contribute only through their contribution to the total charge density, which affects the Hartree and exchange correlation potentials. In contrast in a pseudopotential approach, the Hartree and exchange correlation potentials are obtained from the valence electron density only. However, the 3*s* states lie about 2 Ry below the 3*p* states which already lie at 3 Ry below the VBM. The core-treatment of the 3*s* electrons is thus certainly adequate. The effect of neglecting hybridisation of the 3*p* electrons was studied in Ref. [31]. Treating V-3*p* as core instead of local orbital lowers the QSGW gap by about 0.5 eV while it lowers the LDA

gaps by only 0.2 eV. However, this is not an issue as we do include the V-3*p* orbitals as local orbitals and thus as valence electrons. Thus we can safely conclude that these band structure atomic basis set aspects are adequately treated in both our and Gorelov *et al.*'s calculation. The main difference thus lies in the basis sets used to represent the screening and the Hamiltonian.

For the purpose of visualizing the excitons, we subsequently used a $3 \times 5 \times 5$ mesh because this avoids overlapping exciton wave functions from the periodic images. However, this gives negligible differences in terms of the energy spectrum itself.

In the polarization direction perpendicular to the layers $\mathbf{E} \parallel \mathbf{c}$ we may notice the strong suppression of BSE compared to IPA but also a sharp peak at about 13.5 eV. This was not shown in Ref. [2] because the energy scale was cutoff at lower energy but is also present in that calculation. It can also be seen in Ref. [10] although somewhat less pronounced. The suppression of the imaginary part in the BSE compared to IPA in the energy range up to 10 eV or so, is a result of strong local field effects in layered systems [35]. This is the well-known classical depolarization effect. When a dielectric layer is placed in an external field, it induces a dipole which produces a field opposite to the external field and this reduces the local field inside the layer by the dielectric constant [36]. The sharp peak at 13.5 eV, which lies just above the largest band to band transitions may also be related to local field effects. As discussed in Cudazzo *et al.* [37] for 2D metals and also in an analysis of periodic boundary conditions artifacts in the modeling of local field effects by Tancogne-Dejean *et al.* [38], the imaginary part of the dielectric function $\varepsilon_2(\omega)$ in systems with strong inhomogeneity can resemble the loss function $-\text{Im}[\varepsilon^{-1}(\omega)]$. This then explains both the suppression of the low-energy region of the dielectric function but also the occurrence of a plasmon like peak above the energy range of the band pairs included. This feature is not present in the independent particle approximation and this in itself indicates that it is a local field effect. The sharp peak we see here does not quite look like a plasmon, because the latter is typically much broader. The loss function was in fact calculated for V₂O₅ in Gorelov *et al.* [10]. However, as demonstrated in the Supplemental Material [39] the sharp peak becomes suppressed when we include a higher number of conduction bands $N_c = 30$ instead of $N_c = 20$. In fact, there are similar sharp features at even higher energy and these become suppressed but a sharp feature then still occurs at even higher energy. These in turn are reduced when adding additional valence bands such as the deep lying O-2*s* bands. This indicates that it is the interaction of the sharp plasmon-like feature with the continuum of higher lying electron-hole pairs that leads to a strong plasmon damping. The higher in energy we want to obtain a converged $\varepsilon_2(\omega)$ the higher number of bands are needed in the BSE active space.

3. Macroscopic dielectric constant from $\mathbf{q} \rightarrow 0$ limit

In the results shown in Fig. 3 the limit $\mathbf{q} \rightarrow 0$ of Eq. (4) is taken analytically, which requires to evaluate matrix elements of the commutator $[H, \mathbf{r}]$. For a local potential, these amount to well-known momentum matrix elements.

TABLE II. Indices of refraction $n = \sqrt{\varepsilon_1(\omega = 0)}$ for different directions and in different approximations.

	n_x	n_y	n_z
RPA	1.88	1.83	1.75
BSE $\mathbf{q} \rightarrow 0$	2.37	2.23	1.92
BSE $\mathbf{q} = 0$	2.44	2.42	1.99
Expt. ^a	2.07	2.12	1.97

^aKenny and Kannewurf [4].

However, for the QSGW case, the evaluation of the commutator involves the nonlocal self-energy operator $\tilde{\Sigma}(\mathbf{r}, \mathbf{r}')$, which requires evaluating $\nabla_{\mathbf{k}} \tilde{\Sigma}(\mathbf{r}, \mathbf{k})$ in which the \mathbf{r}' variable is Fourier transformed to reciprocal space [40]. Taking this derivative from the explicit expressions of the self-energy in terms of the LMTO basis functions is cumbersome and in the current implementation of the codes involves some additional approximations, which experience has shown to lead typically to an overestimate of the matrix elements. Alternatively, we may consider directly the dielectric function at small but finite \mathbf{q} , which is obtained as part of the *GW* procedure, and extrapolate numerically to $\mathbf{q} \rightarrow 0$ along the three directions, $\hat{\mathbf{x}} \parallel \mathbf{a}$, $\hat{\mathbf{y}} \parallel \mathbf{b}$ and $\hat{\mathbf{z}} \parallel \mathbf{c}$. This can then be done both at the RPA or the BSE level. This allows us to more accurately evaluate $\varepsilon_1(\omega = 0)$. This amounts to the static value but including only electronic, not phonon contributions, to screening, which is conventionally called ε_∞ . Experimentally, this corresponds to the index of refraction squared at a frequency well below the bands but also well above the phonon frequencies, which we can compare to experimental data by Kenny and Kannewurf [4], who obtained it by extrapolating the behavior of the index of refraction $n(\omega)$ for $\omega \rightarrow 0$ in the region above the phonon bands. This provides an important test of the methodology because good agreement indicates that the QSGW method adequately describes dielectric screening.

Using finite small \mathbf{q} comes with its own set of numerical difficulties. It turns out that to avoid unphysical behavior such as negative values of $\varepsilon_2(\omega)$ it is necessary to replace the bare Coulomb interaction, $4\pi/q^2$, by a Thomas-Fermi screened $4\pi/(q^2 + q_{\text{TF}}^2)$ with a small q_{TF} . We thus need to extrapolate both $\mathbf{q} \rightarrow 0$ and $q_{\text{TF}} \rightarrow 0$. Details of this procedure are given in the Supplemental Material [39]. The main results for the index of refraction are given in Table II.

We can see that the RPA calculated dielectric constants are systematically lower than the BSE calculated ones and the RPA is clearly seen to underestimate the experimental values. The BSE results obtained with the numerical extrapolation are slightly smaller than the ones obtained with the analytically calculated matrix elements, which we call $\mathbf{q} = 0$ instead of $\mathbf{q} \rightarrow 0$. The values for *a* and *b* direction are close but in inverse order from the experiment and larger than for the *c* direction but for the *c* direction the analytically calculated value is closer to the experiment than the numerical extrapolation while the opposite is true for the in-plane directions. This illustrates the numerical difficulties with either approach. Nonetheless, overall the error in the indices of refraction is at most 15%.

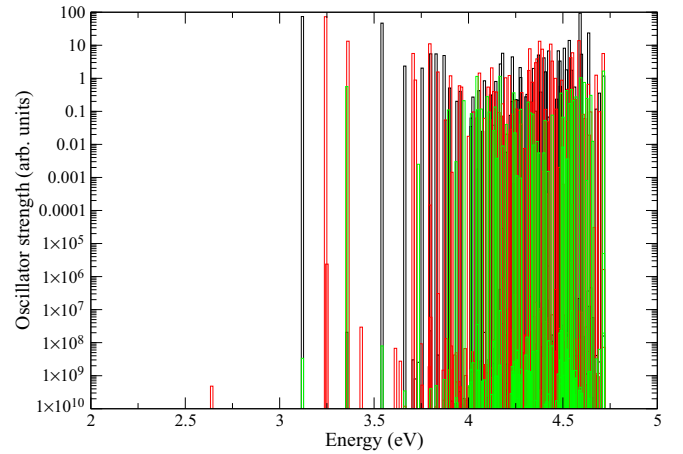


FIG. 4. Eigenvalues of the two particle Hamiltonian with relative oscillator strengths on a log scale. The colors indicate polarization: (black) $\mathbf{E} \parallel \mathbf{a}$, (red) $\mathbf{E} \parallel \mathbf{b}$, and (green) $\mathbf{E} \parallel \mathbf{c}$.

4. Exciton analysis

Besides the bright excitons, there are also several dark excitons. An overview of the eigenvalues of the two-particle Hamiltonian up to about the quasiparticle gap is shown in Fig. 4 as a set of bar graphs with the oscillator strengths on a log scale. (Note that these were obtained with $N_v = 30$ and $N_c = 30$ but for these low-energy excitons the results are equivalent for $N_c = 20$.) Any level which has an oscillator strength lower than 0.1 may be considered dark as it is 1000 times smaller than the bright exciton oscillator strengths. These oscillator strengths are not normalized and thus given in arbitrary units. Only their relative value is important here. It is notable that an approximately doubly degenerate very dark exciton occurs well below the first bright excitons and near 2.6 eV. As was already mentioned in Ref. [2] these result from a destructive interference of the exciton eigenstates at symmetry equivalent \mathbf{k} points rather than from zero dipole matrix elements at each individual \mathbf{k} .

We study the composition of the excitons in various ways. First, we show the bands that contribute significantly to a given exciton λ by selecting a narrow energy window containing just one exciton eigenvalue and by plotting $W_{v\mathbf{k}}^\lambda = \sum_c |A_{v\mathbf{c}\mathbf{k}}^\lambda|^2$ as a color weight on the band plot, where the sum is over *c*, when plotting the weight on the valence band *v*. Similarly, $W_{c\mathbf{k}}^\lambda = \sum_v |A_{v\mathbf{c}\mathbf{k}}^\lambda|^2$ gives the weight on the conduction bands. These are shown in the first row of Figs. 5(a)–5(c) for different excitons of interest. Next, in $\Psi^\lambda = \sum_{v\mathbf{c}\mathbf{k}} A_{v\mathbf{c}\mathbf{k}}^\lambda \psi_{v\mathbf{k}}^h \psi_{c\mathbf{k}}^e$, we can expand the Bloch functions $\psi_{v\mathbf{k}}$ into the muffin-tin-orbital basis functions in a Mulliken analysis, and sum these over angular momenta per atom to obtain a contribution per atom and hence per atom pair of the exciton. The \pm superscript indicates the hole or electron atom location. This is a fully real space analysis. In other words, an inverse Fourier sum is applied to the LMTO basis Bloch functions depending on the \mathbf{k} mesh used. For a $N \times N \times N$ \mathbf{k} mesh, we obtain contributions in a $N \times N \times N$ supercell in real space. We select the most important contributions and indicate them as a percentage on a pie chart in the second row [Figs. 5(d)–5(f)]. For example $V^-O_c^+$ means all contributions

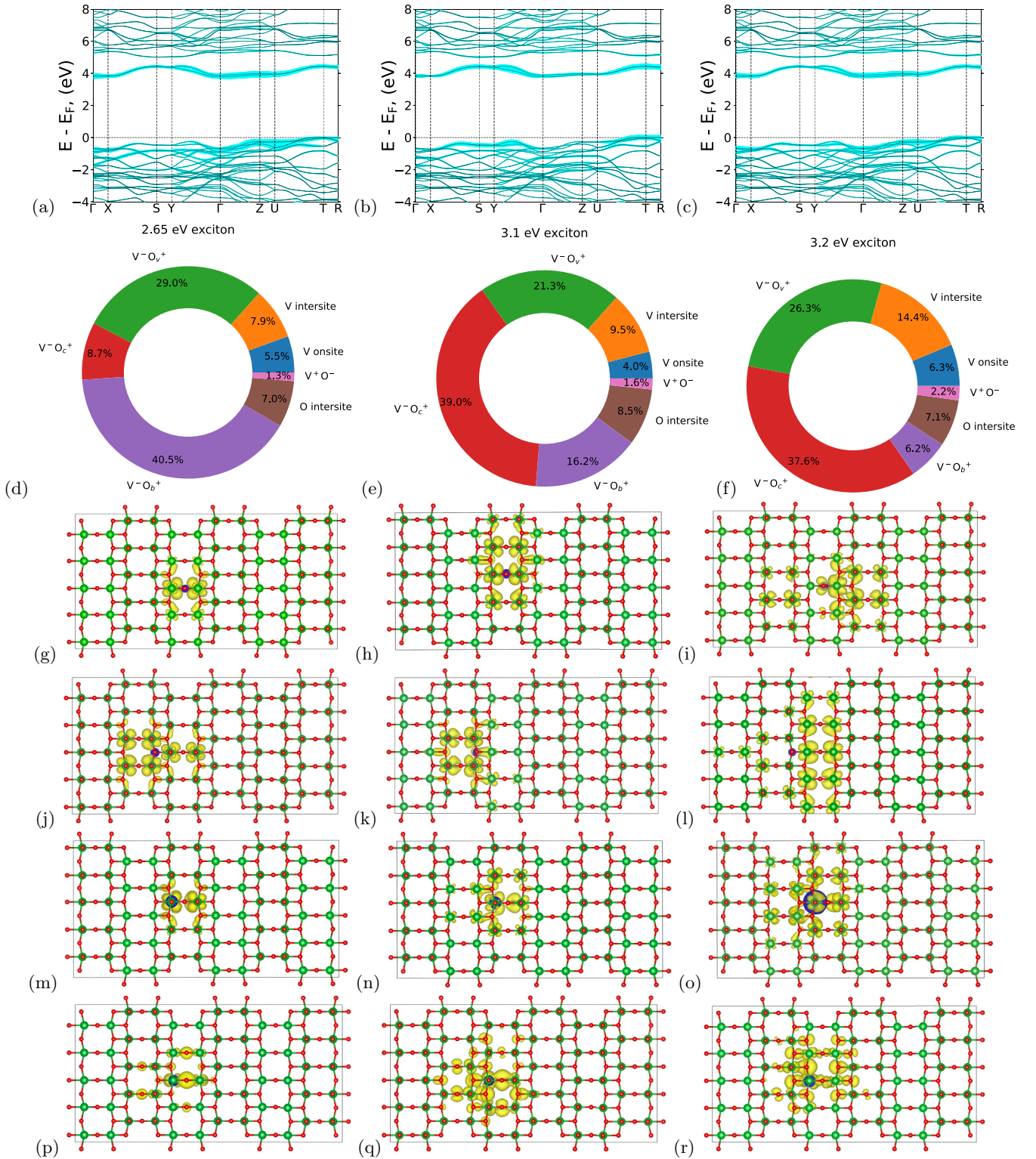


FIG. 5. Exciton wave-function analysis: Panels (a)–(c) give the exciton weight $W_{v(c)k}^\lambda$ along symmetry lines; panels (d)–(f) give integrated decompositions on atom pairs as a pie-chart; panels (g)–(i) give real space figures as function of \mathbf{r}_e when hole is placed on the O_b , panels (j)–(l) on O_c , panels (m)–(o) on O_v , and panels (p)–(r) as function \mathbf{r}_h when electron is fixed at V . The location of the fixed hole or electron is indicated by the blue sphere. Cases (a), (d), (g), (j), (m), and (p) refer to the dark 2.65-eV exciton, (b), (e), (h), (k), (n), and (q) to the 3.1-eV $\mathbf{E} \parallel \mathbf{a}$ bright exciton, and (c), (f), (i), (l), (o), and (r) for the 3.2-eV $\mathbf{E} \parallel \mathbf{b}$ bright exciton.

from an electron on a V and a hole on an O_c regardless of the relative position of the two atoms. Third, we can pick a location for the hole and then display the probability to find the electron around it as a isosurface or fix the electron and visualize the hole distribution. We here analyze the dark exciton at 2.65 eV, the $\mathbf{E} \parallel \mathbf{a}$ bright exciton at 3.1 eV and then the 3.2 eV $\mathbf{E} \parallel \mathbf{b}$ exciton from left to right.

First, from the band weight plots, we can see that all three excitons are derived primarily from the top valence band and lowest conduction band with some smaller contributions from bands farther away from the band edges. They are very spread out in \mathbf{k} space, and hence localized in real space. The localization in real space depends somewhat on the arbitrary choice of isosurface value cutoff which we pick around 10%. Nonetheless they are spread in real space over a few neighbor distances in each direction. One can see from the band plots that the exciton weights are slightly different for the three excitons. For example, the $\mathbf{E} \parallel \mathbf{a}$ exciton had a stronger contribution from UTR and $SY\Gamma$ lines while the $\mathbf{E} \parallel \mathbf{b}$ exciton has larger contributions from $X\Gamma ZU$. The dark exciton is even more equally spread in \mathbf{k} space and hence even more localized in real space. This is consistent with a similar analysis by Gorelov *et al.* [2].

The atom pair analysis shows that the exciton weights stem primarily from electrons on V and holes on the various O. This is consistent with the band analysis, since the lowest conduction bands are V-O antibonding states and have primarily V-3d content, while the top valence bands are V-O bonding states and have primarily O-2p content. It is interesting that the different O do not contribute equally. For the dark exciton, the primary contribution is from the O_b ($\sim 40\%$) with a small contribution from chain oxygens ($\sim 9\%$ and $\sim 30\%$) of the vanadyl O. This distribution occurs in spite of the fact that each V has one O_v , three O_c neighbors and only one O_b is shared by two V across a bridge. For the bright excitons, instead we see primarily contribution around 40% from the chain O and only a small contribution (about 16% and 6% for \mathbf{a} and \mathbf{b} directions, respectively) from the bridge O and around 21–26% of the vanadyl oxygen.

We next show the real space figures for each exciton when the hole is fixed on O_b , O_c , and O_v and when the electron is fixed on V. We can compare the 3.1- and 2.65-eV excitons for the hole fixed on the bridge O with the work of Gorelov *et al.* [2]. In that paper the exciton appeared more extended in the \mathbf{a} direction perpendicular to the chains, and a simple tight-binding model with exciton wave functions centered on the V- O_b -V bridge was developed to understand their spread, comparing in particular the dark and the bright exciton for $\mathbf{E} \parallel \mathbf{a}$ as even and odd partners to each other in their \mathbf{k} and $-\mathbf{k}$ components. In retrospect that model, while instructive, may be somewhat oversimplified [41,42].

One might ask to what extent the real space distributions are sensitive to the precise location of the fixed hole (or electron). The code used to make these figures snaps the position we give as input to the nearest grid point in the real space mesh and this can sometimes be slightly off from the more symmetric atom position we target. For example, Fig. 5(i) appears to have the electron distribution skewed to the right of the bridge O. Nonetheless in Figs. 5(g) and 5(h) we choose the exact same hole location and yet these

appear more symmetric. On the other hand, in Figs. 5(k) and 5(l) we use the same O_c position and yet for the 3.1-eV exciton the wave function spreads more to the left and for the 3.2 eV one more to the right. In view of their different \mathbf{k} -space localization, these appear to be genuine differences between these excitons and not just artifacts of the precise location of the fixed particle in the exciton and we further tested that they are robust to small displacements of the assumed hole position. Complementary information is gained by fixing the electron on a V and examining the corresponding hole distribution. These are shown in Figs. 5(p)–5(r). In these figures we can recognize the O - p like character, while in the previous ones, we can recognize the d_{xy} like character on V.

The consistent picture that emerges from these various visualizations is that the dark exciton at 2.65 eV is significantly more localized than the two bright excitons considered here. They have a rather complex distribution spread over a size of about 5–15 Å and are charge transfer like excitons. Overall, these examples confirm the main finding from Gorelov *et al.* [2] that the excitons are not Frenkel excitons, which one might expect to stay localized on a single atom or molecular fragment like the V- O_b -V bridge, but are more spread out than one would expect for such large exciton binding energies. However, they are more complex than previously thought. Similar strongly anisotropic (almost unidirectional) and strongly bound excitons have been observed in the puckered two-dimensional magnet CrBrS [43,44]. Much as the strongly bound excitons in V_2O_5 those excitons also extend up to ~ 3 to 4 unit cells. However, in strong contrast to the excitons in V_2O_5 , excitons in CrBrS originate from partially filled d -states and are magnetic in nature and have both large on-site dd and significant intersite dipole dp characters [45] to them. The V_2O_5 excitons, however, have barely any onsite components and mostly share the electrons and holes on the V-O (dp) dipole. In other words, as already pointed out by Gorelov *et al.* [2] they can be viewed as charge-transfer excitons. It is in that sense that these excitons are significantly different from dd Frenkel excitons as observed in several strongly correlated ferro- and antiferromagnets [46,47].

B. Monolayer

1. Quasiparticle and optical gaps

Having established good agreement with prior work for V_2O_5 in spite of some differences, we move on to study the monolayer. To calculate the monolayer, we simply increase the distance between the V_2O_5 layers by increasing the c -lattice constant and keeping the layer atomic positions fixed. Using the z coordinate difference between the vanadyl oxygens sticking out on either side of the layer as a measure of the thickness of the layer, the layer has a thickness of 4.096 Å. The c lattice constant is 4.368 Å and the V- O_v vertical distance is 1.575 Å, so between the O_v of one layer and the V above it in the next layer, the distance is 2.793 Å. When we set the $c_{\text{mono}} = a_{\text{bulk}}$ the vacuum thickness is 7.416 Å and the distance from the O_v to the next layer V is 9.9 Å. Using $c_{\text{mono}} = 1.5a_{\text{bulk}}$ the vacuum layer is 13.17 Å and the vertical distance from the O_v to the V above it is 15.69 Å. These seem sufficiently large to represent well isolated monolayers from the point of view of having negligible hopping between the

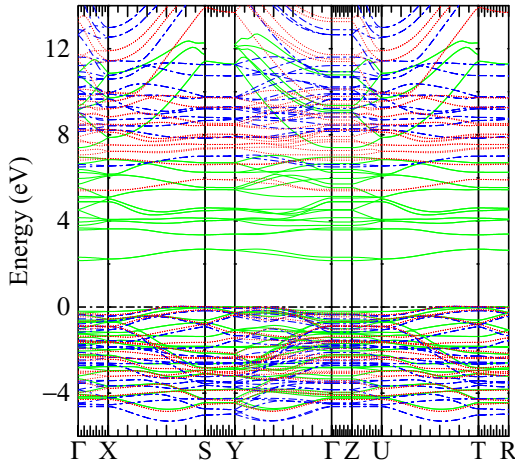


FIG. 6. Band structure of monolayer V_2O_5 in GGA (green solid line), QSGW (blue dot-dashed), and $QSG\hat{W}$ (red dotted) for $c/a = 1.5$.

layers. In fact, we will show that by this distance the GGA gap is well converged but the QSGW gap is not. The band structure of the monolayer using $c_{\text{mono}} = 1.5a_{\text{bulk}}$ is shown in Fig. 6. Note that strictly speaking for a monolayer with infinite separation, the Brillouin zone edge in the c -direction $k_z = \pi/c$ should go to zero. However, by showing the bands also in the $k_z = \pi/c$ plane, $ZUTR$, we show explicitly how flat the bands are along the c direction for the c/a used. The bands in the $ZUTR$ plane are then equal to the ΓXSY and the extent to which this is true indicates whether the c distance is large enough to avoid interlayer hopping. To check the convergence of the gaps we plot the direct and indirect band gaps as function of a/c in Fig. 7 and use a linear extrapolation of the QSGW gaps in the range where the behavior does indeed become linear.

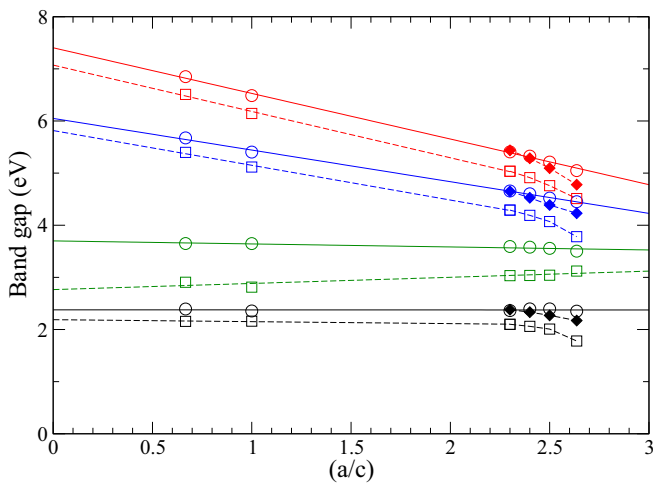


FIG. 7. Quasiparticle gaps in V_2O_5 : Direct gap at Γ (circles) lowest direct gap (diamonds), and indirect gap (squares), as function of a/c , in GGA (black), QSGW (red), and $QSG\hat{W}$ (blue) with straight line interpolations in the linear region; lowest exciton gap for $\mathbf{E} \parallel \mathbf{a}$ in BSE (green) using either QSGW (solid line), or $QSG\hat{W}$ self-energy (dashed line).

The band structure plot Fig. 6 shows that already at the GGA level, the indirect gap is slightly increased compared to the bulk, primarily because the highest valence band in the $TRUZ$ plane (at $k_z = \pi/c$) is now almost the same as in the ΓXSY plane (at $k_z = 0$). The upward dispersion from Γ -Z in the bulk case is missing. This indicates that this dispersion is related to the interlayer hopping interaction in the bulk. Several changes happen in the band structure: the smallest direct gap, which in bulk occurs at Z now occurs at Γ because the bands along the Γ -Z direction become flat. Second, the indirect gap, which in bulk occurs between the VBM at or near T and the CBM at Γ now shifts to a point between X-S and Γ . The self-energy shifts are significantly higher than in the bulk.

In Fig. 7, we can see that these changes occur as soon as the layers become decoupled already for a modest increase in interlayer distance ($a/c = 2.3$ or $c = 5 \text{ \AA}$). The smallest direct gap becomes equal to the direct gap at Γ and in the GGA, the band gaps have essentially converged at this point and stay constant. On the other hand, the QSGW and $QSG\hat{W}$ gaps keep on increasing linearly as we further increase c . This slow convergence with the size of the vacuum region is caused by the long-range nature of the self-energy Σ which is proportional to the screened Coulomb interaction $1/\epsilon r$ because of the screened exchange term. With increasing size of the vacuum the effective dielectric constant of the system becomes smaller. Effectively, the long-range part of the Coulomb interaction becomes unscreened and dominated by the vacuum or surrounding medium for a thin 2D system. This is well known since the work of Keldysh [25] and discussed in detail in Cudazzo *et al.* [24]. The monolayer is thus predicted to have a significantly higher gap than bulk layered V_2O_5 . The linearly extrapolated direct quasiparticle gaps are 7.4 and 6.1 eV in the QSGW and $QSG\hat{W}$ approximations. The difference between direct and indirect gap stays approximately constant as we increase c . Also, the difference between QSGW and $QSG\hat{W}$ stays more or less constant.

On the other hand, the BSE optical gap stays almost constant. The lowest optical gap shown in Fig. 7 is for $\mathbf{E} \parallel \mathbf{a}$ and is a mixture of various direct interband transitions spread throughout \mathbf{k} space. It is not dominated by the lowest gap direct gap (which is at Z in the bulk case) as we have seen in Fig. 5. It does not show the initial increase of the direct and indirect gaps as we start increasing c . It also does not increase as the QSGW gaps. This is because the exciton binding energy is also proportional to W and hence an increase in W due to lower screening results both in an increased self-energy and quasiparticle gap but is compensated by an increased exciton binding energy. The optical gap is thus expected to change only minimally. This applies both when we use W or \hat{W} . In the latter case, the gap seems to go slightly down for larger c , but this is within the error bar. It might indicate that the increase in \hat{W} with c/a is more directly reflected in the exciton binding energy than in the quasiparticle self-energy. This also implies that the exciton gap will be less affected by substrate dielectric screening if the monolayer is placed on top of a substrate. Our optical calculations only provide the excitons derived from direct transitions and the bound excitons are a mixture of vertical band-to-band transitions spread over the whole Brillouin zone. Therefore, the lowest exciton gap (green lines)

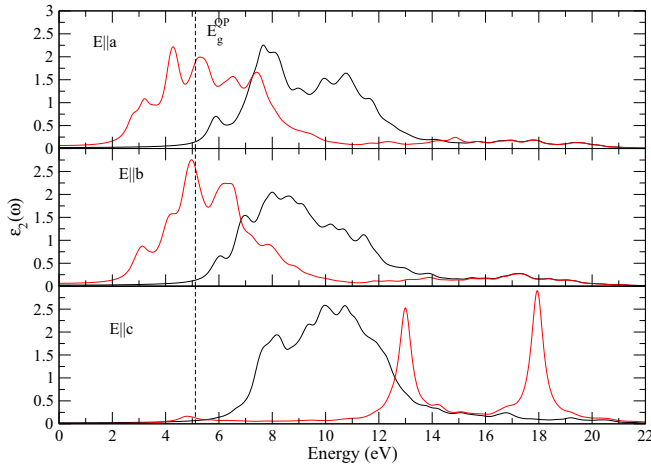


FIG. 8. Imaginary part of the dielectric function in IPA and BSE for the monolayer limit $c/a = 1.5$

does not show the rapid increase with increasing c/a starting from the bulk values. There should also be an indirect exciton related to the indirect excitation of an electron-hole pair via a combined photon and phonon interaction in second order perturbation theory and modified by the electron-hole interaction. At present we cannot calculate this but expect it to follow the dependence of the indirect quasiparticle gap as function of interlayer distance. In fact, this indirect gap changes \mathbf{k} -point location and thus the character of the corresponding exciton will also change. Assuming that the exciton binding energies of direct and indirect excitons are similar we note that the indirect quasiparticle gap between bulk and monolayer changes by about 0.1 eV and hence we expect a similar change in indirect exciton with interlayer distance.

Next we examine the dielectric functions of the monolayer representative cells as function of interlayer distance in Figs. 8 and 9 in some more detail. First, in Fig. 8 we can now see an even stronger suppression of the $\varepsilon_2(\omega)$ in the BSE for $\mathbf{E}||\mathbf{c}$. Again, at higher energies, sharp features occur for the

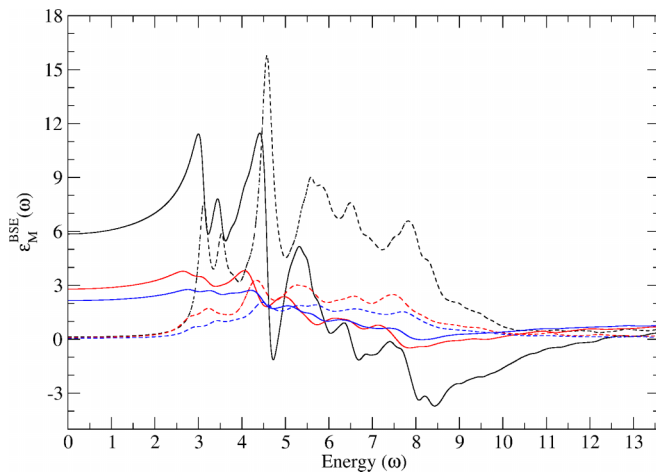


FIG. 9. Real and imaginary part of the dielectric function for polarization $\mathbf{E} || \mathbf{a}$ as function of interlayer spacing; solid lines: ε_1 , dashed lines ε_2 ; bulk (black), $c/a = 1$ (red), and $c/a = 1.5$ (blue).

polarization perpendicular to the layers but these are dismissed as unrealistic artifacts from the BSE active space truncation. This indicates that the local field effects are even stronger in the monolayer case. The excitons are still prominent for the in-plane polarizations, but the lowest peaks still occur near 3.0 eV not too far from the bulk case. Still, the shape of the $\varepsilon_2(\omega)$, i.e., the exciton spectrum, is significantly different from the bulk case.

Next we look a little more closely at the change in dielectric functions, both real and imaginary parts, as function of interlayer spacing in Fig. 9. We can see first of all that the amplitude of the $\varepsilon_2(\omega)$ and the values of $\varepsilon_1(\omega = 0)$ are much reduced in the monolayer cases compared to the bulk and increasingly more so as the thickness of the vacuum layer increases. This can simply be understood in terms of a model of capacitors in series. Essentially, there is a thicker and thicker region of relative dielectric constant 1 in between the layers. Since the capacitance is inversely proportional to its thickness d and proportional to the dielectric constant in that region, the effective dielectric constant can be obtained from adding the capacitance of the layer and of the vacuum region in series, which gives

$$\frac{c}{\varepsilon_{\text{eff}}} = \frac{c_b}{\varepsilon} + \frac{c - c_b}{1}, \quad (7)$$

where c_b is the c -lattice constant for bulk and c the one in the monolayer model. In the limit $c \rightarrow \infty$ this goes to 1, the dielectric constant of vacuum, and in the limit $c \rightarrow c_b$ it gives $\varepsilon_{\text{eff}} = \varepsilon$ of bulk V_2O_5 . We caution that these dielectric functions of the periodically repeated layers do not represent the true dielectric screening behavior inside an isolated monolayer but rather that of the overall system including vacuum. For $c \rightarrow \infty$ the overall dielectric function would go to 1 as it becomes dominated by vacuum. On the other hand the screening in two dimensions becomes strongly distance dependent with qualitatively different behavior at distances smaller than the thickness of the layer and larger than it, as is well known since the work of Keldysh [25] and Cudazzo *et al.* [24].

The real space spread of the first bright exciton for $\mathbf{E} || \mathbf{a}$ in the monolayer is shown in Fig. 10 for the hole placed on the bridge O_b and as function of electron position. It looks quite similar to that in the bulk case, shown in Fig. 5(h). The difference is it that is entirely confined to one monolayer while in the bulk case, it spreads slightly to neighboring layers. This is not visible in the projection figures here but can be ascertained by viewing the exciton wave function from different angles. Its spread in \mathbf{a} direction appears slightly larger here than in Fig. 5(h) but this is because we here used a $2 \times 5 \times 1$ mesh. Apparently two \mathbf{k} points in the \mathbf{a} direction is not yet sufficient to completely avoid overlap of the excitons in adjacent cells from the periodic boundary conditions in the \mathbf{a} direction. We note that similar to the bulk, dark excitons also exist at lower energy for the monolayer. In Fig. 11 we show the oscillator strengths of the exciton eigenvalues up to 4 eV on a log scale. Similar to the bulk case, we find a pair of dark excitons near 2.48 and 2.49 eV, while the first bright excitons occur at 2.91 and 3.03 eV for $\mathbf{E} || \mathbf{a}$ and $\mathbf{E} || \mathbf{b}$, respectively. Surprisingly, these lie actually slightly lower than the bulk case, even though the quasiparticle gap was strongly increased. This is

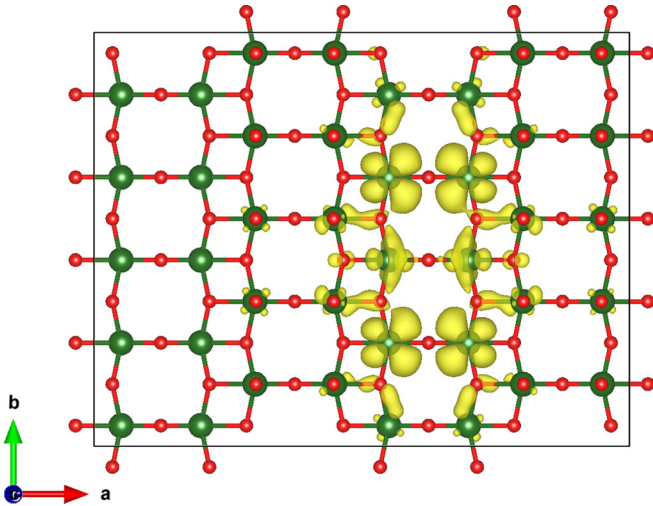


FIG. 10. First bright exciton $E_{||a}$ in monolayer V_2O_5 for the hole place on the bridge oxygen as function of electron position and calculated for $c/a = 1.5$.

consistent with the slight decrease for increasing c seen in Fig. 7 for the QSGW case.

2. Comparison to experiment

Monolayer V_2O_5 has not yet been realized although attempts at exfoliation have resulted in ultrathin layers of order 8–10 atomic layers thick [48]. Only recently, layers as thin as bi- or trilayer of V_2O_5 were realized by sonification after swelling of the interlayer distance by intercalation with formamide molecules as reported by Reshma *et al.* [49]. These studies showed an increase in optical absorption edge by about 1.3 eV for the thinnest samples which contained individual layers of order 1.1–1.5 nm, corresponding to two to three layers. It is not straightforward to interpret the onset of the Tauc plot as the direct gap because of the large excitonic effects and disorder related band tailing effects. The Tauc plot prediction of an absorption coefficient proportional to $\sqrt{E - E_{\text{gap}}}$ for direct allowed transitions is valid only for band to band

transitions. However, including polaritonic effects it may also correspond to indirect excitons [50]. The value reported for bulk in Ref. [49] is 2.39 eV, which is close to the gap reported by Kenny and Kannewurf [4] but much smaller than the direct excitonic peak seen in spectroscopic ellipsometry [2]. See also Fig. 3. Thus, the Tauc-plot onsets more likely correspond to an indirect exciton but may also be influenced by defects. While the direct exciton gap is not expected to vary significantly with layer separation according to our present calculations, because such excitons are a mixture of band to band transitions at different \mathbf{k} points, and because of the compensation of exciton binding energy and gap shift, the indirect gap exciton might have a somewhat higher binding energy and be more localized in \mathbf{k} space. For the bulk we obtain a lowest direct gap at 4.2 eV and the lowest bright exciton is at 3.1 eV, indicating an exciton binding energy of $E_B \approx 1.1$ eV. Assuming that an indirect exciton associated with the indirect gap of 3.8 eV has a similar binding energy, we would find the optical indirect exciton gap in bulk at about 2.7 eV. This is still 0.3 eV larger than the onset of the Tauc plot in Ref. [49]. Thus we hypothesize that the exciton binding energy is larger for the indirect exciton. Nonetheless, we might expect the indirect exciton to more closely follow a specific band edge and thus increase slightly with increasing layer separation. Furthermore the nature of the indirect transition changes to another \mathbf{k} location of the VBM and the difference between direct and indirect quasiparticle gap is reduced from that in bulk. Similar changes in direct/in-direct nature of the band gap going from the bulk to the monolayer limit are observed in several layered vdW systems [51,52]. We may thus expect that for monolayers the optical gap even if still indirect might approach more closely the direct gap exciton. Still our calculations of the indirect band gap shift between bulk and monolayer indicate this shift would be of only 0.3 eV or so, which is significantly smaller than what is reported in Ref. [49]. To better understand this discrepancy it will be necessary to calculate indirect exciton gaps and to obtain a more detailed experimental analysis of monolayer optical properties.

IV. CONCLUSIONS

In this paper we presented all-electron quasiparticle band structure calculations using a modified QSGW method, and optical response function calculations using the BSE approach. The inclusion of ladder diagrams in calculating the polarization function which determines the screened Coulomb interaction W of the GW method is shown to reduce the self-energy correction of the gap beyond DFT by about a factor 0.77. Our quasiparticle band gaps for the bulk including these electron-hole effects are in good agreement with the literature using a pseudopotential implementation but without this electron-hole reduction of the W . Because of this somewhat fortuitous agreement on the quasiparticle gap, in spite of the different approximations made in the calculation of W , we then find the excitons and imaginary part of the dielectric function to also be in good agreement with prior work for bulk. There thus remains some discrepancy on how to obtain the correct W but once W is established, good agreement is obtained in band structures and optical dielectric response. Some effects of the strong local field effects in the direction

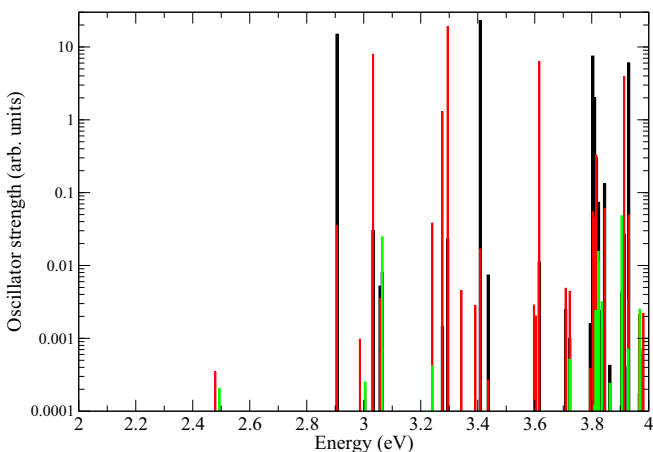


FIG. 11. Relative oscillator strengths of exciton eigenvalues for the monolayer case $c/a = 1.5$ on a log scale: Black, red, and green correspond to a , b , and c polarizations.

perpendicular to the layers were observed here and the appearance of unphysical high-energy sharp peaks was shown to be an artifact of the truncation of the active space in the BSE. Finally, the electronic screening only static dielectric constant was evaluated using an extrapolation from finite \mathbf{q} and found to give good agreement for the indices of refraction with experiment to within about 15%. This confirms that in the QSGW approach both the band gaps and the screening are consistently in good agreement with experiment.

For monolayers, we find an increased quasiparticle gap but slow convergence of the quasiparticle gap with the distance between the layers, as observed in other 2D systems. On the other hand, the optical direct exciton gap converges much faster because as the quasiparticle gap increases, so increases the exciton binding energy because both are proportional to W , which is increased by reduced screening in a 2D system. The local field effect perpendicular to the layer were found to be even stronger in the monolayer than in the bulk. While the direct gap at Γ does not change much between bulk and monolayer at the GGA level, the top valence band becomes flattened out and this increases both the smallest direct gap at Z and the indirect gap. Assuming a similar exciton binding energy for the (not yet calculated) indirect exciton as for the direct excitons, we predict a slight increase of the optical absorption onset in monolayers. An increase in optical gap was recently observed for exfoliated two- to three-layer-thin

samples but was found to exhibit larger shifts than we here predict.

The data pertaining to various figures are available at Ref. [53]. In particular, XCRYSDEN [54] (.xsf) and VESTA [55] (.vesta) datafiles related to Fig. 5 $g-r$ are available to facilitate 3D viewing.

ACKNOWLEDGMENTS

This work was supported by the U. S. Department of Energy Basic Energy Sciences (DOE-BES) under Grant No. DE-SC0008933. Calculations made use of the High Performance Computing Resource in the Core Facility for Advanced Research Computing at Case Western Reserve University. S.A. is supported by the Computational Chemical Sciences program within the U.S. DOE, Office of Science, BES, under Award No. DE-AC36-08GO28308. S.A. used resources of the National Energy Research Scientific Computing Center, a DOE Office of Science user facility supported under Award No. DE-AC02-05CH11231 using NERSC Award No. BES-ERCAP0021783. We thank V. Gorelov and coauthors of Ref. [2] for providing the numerical data of their calculations and for useful discussions. We also thank D. Pashov for his many contributions to the codes used here.

-
- [1] S. K. Radha, W. R. L. Lambrecht, B. Cunningham, M. Grüning, D. Pashov, and M. van Schilfgaarde, Optical response and band structure of LiCoO_2 including electron-hole interaction effects, *Phys. Rev. B* **104**, 115120 (2021).
- [2] V. Gorelov, L. Reining, M. Feneberg, R. Goldhahn, A. Schleife, W. R. L. Lambrecht, and M. Gatti, Delocalization of dark and bright excitons in flat-band materials and the optical properties of V_2O_5 , *npj Comput. Mater.* **8**, 94 (2022).
- [3] V. Eyert and K.-H. Höck, Electronic structure of V_2O_5 : Role of octahedral deformations, *Phys. Rev. B* **57**, 12727 (1998).
- [4] N. Kenny, C. Kannewurf, and D. Whitmore, Optical absorption coefficients of vanadium pentoxide single crystals, *J. Phys. Chem. Solids* **27**, 1237 (1966).
- [5] C. Bhandari, W. R. L. Lambrecht, and M. van Schilfgaarde, Quasiparticle self-consistent *GW* calculations of the electronic band structure of bulk and monolayer V_2O_5 , *Phys. Rev. B* **91**, 125116 (2015).
- [6] S. Lany, Band-structure calculations for the $3d$ transition metal oxides in *GW*, *Phys. Rev. B* **87**, 085112 (2013).
- [7] M. J. van Setten, M. Giantomassi, X. Gonze, G.-M. Rignanese, and G. Hautier, Automation methodologies and large-scale validation for *GW*: Towards high-throughput *GW* calculations, *Phys. Rev. B* **96**, 155207 (2017).
- [8] V. G. Mokerov, V. L. Makarov, V. B. Tulvinskii, and A. R. Begishev, Optical properties of vanadium pentoxide in the region of photon energies from 2 eV to 14 eV, *Opt. Spectrosc.* **40**, 58 (1976).
- [9] M. Losurdo, G. Bruno, D. Barreca, and E. Tondello, Dielectric function of V_2O_5 nanocrystalline films by spectroscopic ellipsometry: Characterization of microstructure, *Appl. Phys. Lett.* **77**, 1129 (2000).
- [10] V. Gorelov, L. Reining, W. R. L. Lambrecht, and M. Gatti, Robustness of electronic screening effects in electron spectroscopies: Example of V_2O_5 , *Phys. Rev. B* **107**, 075101 (2023).
- [11] T. Kotani, M. van Schilfgaarde, and S. V. Faleev, Quasiparticle self-consistent *GW* method: A basis for the independent-particle approximation, *Phys. Rev. B* **76**, 165106 (2007).
- [12] D. Pashov, S. Acharya, W. R. Lambrecht, J. Jackson, K. D. Belashchenko, A. Chantis, F. Jamet, and M. van Schilfgaarde, Questaal: A package of electronic structure methods based on the linear muffin-tin orbital technique, *Comput. Phys. Commun.* **249**, 107065 (2019).
- [13] C. Friedrich, S. Blügel, and A. Schindlmayr, Efficient implementation of the *GW* approximation within the all-electron FLAPW method, *Phys. Rev. B* **81**, 125102 (2010).
- [14] A. L. Kutepov, Electronic structure of Na, K, Si, and LiF from self-consistent solution of Hedin's equations including vertex corrections, *Phys. Rev. B* **94**, 155101 (2016).
- [15] A. L. Kutepov, Self-consistent solution of Hedin's equations: Semiconductors and insulators, *Phys. Rev. B* **95**, 195120 (2017).
- [16] A. L. Kutepov, Full versus quasiparticle self-consistency in vertex-corrected *GW* approaches, *Phys. Rev. B* **105**, 045124 (2022).
- [17] H. Jiang and P. Blaha, *GW* with linearized augmented plane waves extended by high-energy local orbitals, *Phys. Rev. B* **93**, 115203 (2016).

- [18] B. Cunningham, M. Grüning, P. Azarhoosh, D. Pashov, and M. van Schilfhaarde, Effect of ladder diagrams on optical absorption spectra in a quasiparticle self-consistent *GW* framework, *Phys. Rev. Mater.* **2**, 034603 (2018).
- [19] B. Cunningham, M. Grüning, D. Pashov, and M. van Schilfhaarde, QSGW: Quasiparticle self-consistent *GW* with ladder diagrams in *W*, *Phys. Rev. B* **108**, 165104 (2023).
- [20] M. Shishkin, M. Marsman, and G. Kresse, Accurate quasiparticle spectra from self-consistent *GW* calculations with vertex corrections, *Phys. Rev. Lett.* **99**, 246403 (2007).
- [21] W. Chen and A. Pasquarello, Accurate band gaps of extended systems via efficient vertex corrections in *GW*, *Phys. Rev. B* **92**, 041115(R) (2015).
- [22] L. Hedin, New method for calculating the one-particle Green's function with application to the electron-gas problem, *Phys. Rev.* **139**, A796 (1965).
- [23] L. Hedin and S. Lundqvist, Effects of electron-electron and electron-phonon interactions on the one-electron states of solids, in *Solid State Physics, Advanced in Research and Applications*, edited by F. Seitz, D. Turnbull, and H. Ehrenreich (Academic Press, New York, 1969), Vol. 23, pp. 1–181.
- [24] P. Cudazzo, I. V. Tokatly, and A. Rubio, Dielectric screening in two-dimensional insulators: Implications for excitonic and impurity states in graphane, *Phys. Rev. B* **84**, 085406 (2011).
- [25] L. V. Keldysh, Coulomb interaction in thin semiconductor and semimetal films, *Pis'ma Zh. Eksp. Teor. Fiz.* **29**, 716 (1979) [*JETP Lett.* **29**, 658 (1979)].
- [26] J. P. Perdew, K. Burke, and M. Ernzerhof, Generalized gradient approximation made simple, *Phys. Rev. Lett.* **77**, 3865 (1996).
- [27] R. Starke and G. Kresse, Self-consistent Green function equations and the hierarchy of approximations for the four-point propagator, *Phys. Rev. B* **85**, 075119 (2012).
- [28] E. Maggio and G. Kresse, *GW* vertex corrected calculations for molecular systems, *J. Chem. Theory Comput.* **13**, 4765 (2017).
- [29] T. Kotani, Quasiparticle self-consistent *GW* method based on the augmented plane-wave and muffin-tin orbital method, *J. Phys. Soc. Jpn.* **83**, 094711 (2014).
- [30] R. Enjalbert and J. Galy, A refinement of the structure of V_2O_5 , *Acta Crystallogr. Sect. C* **42**, 1467 (1986).
- [31] C. Bhandari, First-principles study of electronic and vibrational properties of bulk and monolayer V_2O_5 , Ph.D. thesis, Case Western Reserve University, 2016.
- [32] C. Bhandari, M. van Schilfhaarde, T. Kotani, and W. R. L. Lambrecht, All-electron quasiparticle self-consistent *GW* band structures for $SrTiO_3$ including lattice polarization corrections in different phases, *Phys. Rev. Mater.* **2**, 013807 (2018).
- [33] F. Aryasetiawan and O. Gunnarsson, Product-basis method for calculating dielectric matrices, *Phys. Rev. B* **49**, 16214 (1994).
- [34] M. Betzinger, C. Friedrich, A. Görling, and S. Blügel, Precise response functions in all-electron methods: Application to the optimized-effective-potential approach, *Phys. Rev. B* **85**, 245124 (2012).
- [35] M. S. Hybertsen and S. G. Louie, *Ab initio* static dielectric matrices from the density-functional approach. I. Formulation and application to semiconductors and insulators, *Phys. Rev. B* **35**, 5585 (1987).
- [36] G. Onida, L. Reining, and A. Rubio, Electronic excitations: Density-functional versus many-body Green's-function approaches, *Rev. Mod. Phys.* **74**, 601 (2002).
- [37] P. Cudazzo, M. Gatti, and A. Rubio, Local-field effects on the plasmon dispersion of two-dimensional transition metal dichalcogenides, *New J. Phys.* **15**, 125005 (2013).
- [38] N. Tancogne-Dejean, C. Giorgetti, and V. Véniard, Optical properties of surfaces with supercell *ab initio* calculations: Local-field effects, *Phys. Rev. B* **92**, 245308 (2015).
- [39] See Supplemental Material at <http://link.aps.org/supplemental/10.1103/PhysRevB.110.085102> for contains additional information on the active space truncation and the numerical extrapolation of $\mathbf{q} \rightarrow 0$, and is available at the paper's website.
- [40] R. Del Sole and R. Giralda, Optical properties of semiconductors within the independent-quasiparticle approximation, *Phys. Rev. B* **48**, 11789 (1993).
- [41] V. Gorelov and L. Reining pointed out to us in private communication that they carried out a revised analysis of the exciton spread, which now appears to be similar in the directions perpendicular and parallel to the chains and is closer to our present results.
- [42] V. Gorelov, L. Reining, M. Feneberg, R. Goldhahn, A. Schleife, W. R. L. Lambrecht, and M. Gatti, Author correction: Delocalization of dark and bright excitons in flat-band materials and the optical properties of V_2O_5 , *npj Comput. Mater.* **10**, 85 (2024).
- [43] J. Klein, B. Pingault, M. Florian, M.-C. Heißenbüttel, A. Steinhoff, Z. Song, K. Torres, F. Dirnberger, J. B. Curtis, M. Weile, A. Penn, T. Deilmann, R. Dana, R. Bushati, J. Quan, J. Luxa, Z. Sofer, A. Alú, V. M. Menon, U. Wurstbauer *et al.*, The bulk van der Waals layered magnet $CrSBr$ is a quasi-1D material, *ACS Nano* **17**, 5316 (2023).
- [44] Y. Shao, F. Dirnberger, S. Qiu, S. Acharya, S. Terres, E. Telford, D. Pashov, B. S. Y. Kim, F. Ruta, D. G. Chica, Y. Wang, Y. J. Bae, A. J. Millis, M. I. Katsnelson, K. Mosian, Z. Sofer, A. Chernikov, M. van Schilfhaarde, X. Zhu, X. Roy *et al.*, Magnetically confined surface and bulk excitons in a layered antiferromagnet (unpublished).
- [45] F. L. Ruta, S. Zhang, Y. Shao, S. L. Moore, S. Acharya, Z. Sun, S. Qiu, J. Geurs, B. S. Kim, M. Fu *et al.*, Hyperbolic exciton polaritons in a van der Waals magnet, *Nat. Commun.* **14**, 8261 (2023).
- [46] S. Acharya, D. Pashov, A. N. Rudenko, M. Rösner, M. van Schilfhaarde, and M. I. Katsnelson, Real-and momentum-space description of the excitons in bulk and monolayer chromium tri-halides, *npj 2D Mater. Appl.* **6**, 33 (2022).
- [47] S. Acharya, D. Pashov, C. Weber, M. van Schilfhaarde, A. I. Lichtenstein, and M. I. Katsnelson, A theory for colors of strongly correlated electronic systems, *Nat. Commun.* **14**, 5565 (2023).
- [48] S. Sucharitakul, G. Ye, W. R. L. Lambrecht, C. Bhandari, A. Gross, R. He, H. Poelman, and X. P. A. Gao, V_2O_5 : A 2D van der Waals oxide with strong in-plane electrical and optical anisotropy, *ACS Appl. Mater. Interfaces* **9**, 23949 (2017).
- [49] R. P. R. A. Pazhedath, S. K. Sinha, A. Dasgupta, G. Karuppiah, A. K. Prasad, and S. Dhara, Electronic and vibrational decoupling in chemically exfoliated bilayer thin two-dimensional V_2O_5 , *J. Phys. Chem. Lett.* **12**, 9821 (2021).
- [50] R. J. Elliott, Intensity of optical absorption by excitons, *Phys. Rev.* **108**, 1384 (1957).
- [51] M. Wu, Z. Li, T. Cao, and S. G. Louie, Physical origin of giant excitonic and magneto-optical responses in two-

- dimensional ferromagnetic insulators, *Nat. Commun.* **10**, 2371 (2019).
- [52] S. Acharya, D. Pashov, B. Cunningham, A. N. Rudenko, M. Rösner, M. Grüning, M. van Schilfgaarde, and M. I. Katsnelson, Electronic structure of chromium trihalides beyond density functional theory, *Phys. Rev. B* **104**, 155109 (2021).
- [53] Data pertaining to the paper are available at <https://github.com/Electronic-Structure-Group/v2o5-quasiparticle-exciton>.
- [54] XCrysDen is a crystal structure and density visualization program available at <http://www.xcrysden.org>.
- [55] VESTA is a 3D visualization program for structural models and volumetric data available from <https://jp-minerals.org/vesta/en/>.